Implicit treatment of substrate and power-ground losses in return-limited inductance extraction *

Dipak Sitaram†, Yu Zheng, and K. L. Shepard
Department of Electrical Engineering, Columbia University New York, NY
† Cadence Design Systems, New Providence, NJ

Abstract

Full-wave analysis, based on rigorous solution of the differential or integral form of Maxwell's equations, is too slow for all but the smallest designs. Traditional on-chip extraction engines are, therefore, being pushed to extract inductance and provide accurate high-frequency interconnect modelling while maintaining computational efficiency and capacity. This paper describes further accuracy-improving enhancements to the commecial full-chip RLCK extraction engine, Assura RLCX[1], based on the return-limited inductance formulation. Specifically, we incorporate substrate losses due to eddy currents and power-ground losses while, based on design-driven assumptions, avoiding explicit extraction of the power-ground and substrate. Results are validated on small testcases where comparison with full-wave solution is practical.

1 Introduction

With technology scaling, on-chip frequencies are increasing as device f_T values exceed 50 GHz. In digital integrated circuits, slew times are being driven below 50 psec, corresponding to frequency content approaching 10 GHz. For many nets, the clock being the most notable[2], inductance must be included to accurately predict rise and fall times and delays in timing analysis. If an inductive net is overdriven, an underdamped ringing response can be observed, which can result in functional failure in receiving circuits or produce reliability problems through gate oxide stress. Moreover, inductive coupling, along with capacitive coupling, can be a significant source of noise on quiet nets due to the switching of nearby perpetrators.

In analog integrated circuits, on-chip frequencies for wireline and wireless applications are also pushing beyond 10 GHz, in optical communications circuits[3] and in RF circuits[4]. On-chip inductance extraction techniques have already been applied to spiral inductors[5, 6, 7], but on-chip transmission lines are finding places in both distributed feedback amplifiers[8] and oscillators[9]. Increasingly also the parasitic inductance of on-chip interconnect is becoming a concern.

High-frequency interconnect analysis has traditionally been relegated to full-wave Maxwell's equations solvers. Field solvers, such as Ansoft's HFSS, which find broad use in the microwave community, solve the differential form of Maxwell's equations with volume discretization and finite-element techniques. By contrast, boundary-element techniques are integral-equation-based solutions which rely on discretizing the sources. Method-of-moment-based solvers[10], such as Agilent's Momentum, are widely employed in the microwave community. In the IC and package communities, integral-equation-based solution are popularly represented in terms of partial-element equivalent circuits (PEEC) which can be solved with circuit simulation engines[11, 12]. If the coupling distances are short relative to the wavelength (that is, the distances between conductor segments that are magnetically or electrically coupled), then the quasi-static approximation applies and no retardation is necessary in the analysis[13]. Fast integral equation solvers have been developed to provide accurate electrostatic, magnetostatic, and full-wave integral equation solutions[14, 15, 16]. Such solvers, while achieving high accuracy, are still very slow except for the smallest problem sizes and the resulting formulations are still intractably dense for large designs. As a result, parasitic extraction engines, which compromise some accuracy to achieve full-chip capacity, are being pushed to provide quasi-static high-frequency extraction capabilities; that is, the extractors are being extended to add inductance to the more familiar resistance and capacitance effects.

Full-chip extraction engines generally use pattern matching and interpolation from look-up tables to calculate capacitance, look-up tables that are generally calculated with use of fast integral equation solvers. Capacitances have very strong geometry dependence; therefore, considerable care is necessary to achieve accurate values. The extracted capacitances are intrinsically sparse because capacitances are very "short-ranged." Electric field lines effectively terminate on the closest conductors and more distant couplings are negligibly small. Physically, these small capacitances can be discarded without any effect on the passivity of the resulting network.

Inductances, by contrast, have relatively weak geometry dependence, allowing for accurate calculation with relatively simple analytic formulae. Magnetic coupling, however, is dense, leading immediately to circuit-level intractibility for large problem sizes. The inductance matrix is dense physically because magnetic fields induced by a current can spread much further and must be "terminated" by eddy currents induced in nearby conductors. Furthermore, the partial inductance formulation is mathematically dense. Partial inductances are defined by flux areas that extend to infinity. Physically meaningful loop inductances are only obtained when the more distant flux areas are "cancelled" out by distant partial mutual inductances. Small mutual inductances cannot be discarded without disrupting the passivity of the network[17].

There have been two recent approaches proposed to "sparsify" the inductance problem, each with its own advantages and disadvantages[18]. The first approach recognizes that the inverse of the inductance matrix (variously called the K-element[19][1] and the susceptance matrix[20]) is mathematically "local"; that is, one

* The work at Columbia University was supported in part by the National Science Foundation under grant CCR-97-34216

[1] The use of the term K-element was perhaps a poor one since SPICE already defines a K element as simply a (normalized) mutual inductances. We use this definition of K is this paper.

does not have to combine many distant coupling to obtain a physical answer. As such, as for the case of the capacitance matrix, elements can be discarded without disturbing the passivity of the network. While the formulation is now mathematically sparse, the problem is still physically dense and the approach provides no mechanism for determining the interaction window size. The most significant disadvantage of the technique, however, is that existing simulation tools (and designer intuition) are based on the concept of inductance rather than "inverse inductance."

An alternative to the inverse-inductance approach is the approach of return-limited inductance[21] which is employed in Assura RLCX[1]. In this technique, the power-ground network is used to divide the chip into interaction regions. This approach recognizes the fact that power-ground nets are always available as fail-safe high-frequency current returns so that eddy currents in most cases will not be induced significantly beyond the nearest power-ground nets. The power-ground network is modelled *implicitly* in this approach with the power-ground nets acting as virtual ground planes. By implicit, we mean that an equivalent RLCK network is generated for the signal lines which includes the effects of the power-ground lines without requiring an explicit network representation of these wires which could easily result in an intractable analysis. This paper reports two accuracy-improving enhancements to Assura RLCX[1]: the incorporation of power-ground losses and consideration of eddy current losses in the substrate.

Earlier return-limited inductance extraction approaches[1] ignored resistive losses in the power-ground distribution. This assumption is frequently not justified because high-frequency current returns may choose more resistive return paths through power-ground lines to minimize inductance, resulting in a higher effective resistance for the line. These effects are now considered.

In the metal-rich environment of digital integrated circuits, eddy current loss in the substrate is not a concern because the on-chip power supply is always available as a lower impedance current return than the silicon substrate. In analog designs, however, this may not be the case since routed power-ground distributions are more common and a sparse metal environment is often present in which the silicon substrate (particularly if an epitaxial substrate is used) may be the lowest impedance current return, often at the cost of considerable resistive losses. We enhance the extraction to consider these eddy current losses.

Section 2 describes how power-ground losses are considered within the context of return-limited inductance extraction. A multilayer Greens' function approach to handle the magnetostatics of the substrate is described in Section 3. Section 4 considers how the concomitant frequency dependence of the inductance and resistance resulting from both loss mechanisms is handled with frequency-independent elements with an equivalent ladder network fit. Section 5 presents comparison of Assura RLCX extraction results with full-wave solution and considers some of the limitations and assumptions of the approach considered here. Section 6 concludes.

2 Magnetostatic power-ground loss modelling

In return-limited inductance extraction, the power-ground network of the chip is used to divide the interconnect into a set of disjoint interaction regions. Self-inductances are defined by loops formed with the nearest parallel power-ground lines. The reader is referred to References [1, 21] for more details on the return-limited extraction approach. Signal lines within an interaction region are magnetically coupled as loop inductances, and signal lines contained in two different interaction regions do not couple. In this approach, the power-ground lines are implicit in the extraction and when losses in these lines are considered, the resulting signal-line models acquire a frequency-dependence.

We note than an important part of full-wave analysis is understanding the interplay of displacement, conduction, and eddy currents, and this analysis involves the simultaneous quasi-static PEEC extraction of the signal lines and the power-ground distribution. In this context, to get a truly accurate analysis of the high-frequency behavior of the power-ground nets one must correctly model the wires of the distribution as well as all the sources of on-chip decoupling capacitance. Depending on the amount of on-chip decoupling, package modelling might also be necessary. The resulting extraction and analysis easily becomes intractable. A better approach to handle large problem sizes (and that taken in return-limited inductance extraction) is to assume that the power-ground distribution has been well-designed and has a very low impedance compared to the signal lines being analyzed. For power-supply integrity considerations, this is achieved in practice with power-ground grid structures and adequate decoupling capacitance. With the assumption of a low-impedance power-ground distribution, we can ease the full-wave requirements on the power-ground distribution by treating capacitances to power and ground lines as capacitances to ideal ground. Furthermore, eddy currents induced in nearest neighbor power-ground lines can be "sourced" from the power-ground distribution with zero impedance.

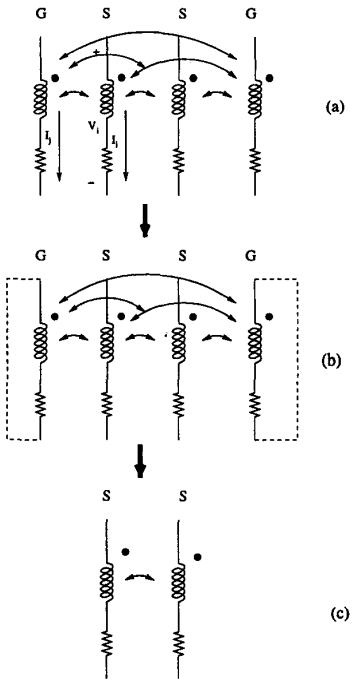

Figure 1: Interaction region cluster defined by a set of signal lines and the associated power-ground lines.

Within Assura RLCX, then, a given interaction region consists of a set of "clusters"; each cluster contains a set of signal lines and their associated parallel power-ground lines (referred to as the power-ground aggregate) which define the return-limited loop inductances. One such cluster is shown in Figure 1(a). The current flowing through the I signals lines of the cluster is given by I_i, giving voltage drops of V_i. The current flowing through the J ground returns is given by I_j. Each cluster is also augmented by a "pseudoreturn" to crudely model all of the (low-resistance, but high-inductance) current returns outside the interaction region; this enables a frequency-dependent transition from a dc resistance defined only by the resistance of the signal line (power grid is lossless at dc) to a high-frequency resistance defined by returns confined to the interaction region. Low frequency inductances are not correctly modelled, but they have no significance in determining interconnnect response. The currents and voltages are related by an impedance matrix:

$$\boldsymbol{V} = \boldsymbol{Z}\boldsymbol{I}$$

where $\boldsymbol{Z}$ is given by $\boldsymbol{R} + j\omega\boldsymbol{L}$. $\boldsymbol{R}$, as the resistance matrix, is diagonal. $\boldsymbol{L}$ is the dense matrix of partial inductances. For simplicity, the remainder of the discussion assumes that the interaction region consists of a single cluster; but the derivation can be easily generalized to multiple clusters in the interaction region.

$\sum_j I_j = I_g = -(\sum_i I_i)$ since the (net) current being driven down the signal lines of the cluster must be returning (implicitly) through the power-ground lines. From this and the assumption of a low-impedance power-ground distribution (shown by the shunts across the power-ground nets in Figure 1(b)), we see that

$$\begin{pmatrix} I_i \\ I_g \end{pmatrix} = \boldsymbol{B}\boldsymbol{Z}^{-1}\boldsymbol{B}^T \begin{pmatrix} V_i \\ 0 \end{pmatrix} \tag{1}$$

where $\boldsymbol{B}$ is an incidence matrix. Each column of $\boldsymbol{B}$ corresponds to a signal line or a power-ground line; each row of $\boldsymbol{B}$ corresponds to a signal line or power-ground line aggregate in one cluster. The ith column of B is all zero except for the ones in rows corresponding to the same signal line or the aggregate containing the power-ground line.

Inverting the current-voltage relation yields:

$$\begin{pmatrix} \mathbf{V}_i \\ 0 \end{pmatrix} = (\boldsymbol{B}\boldsymbol{Z}^{-1}\boldsymbol{B}^T)^{-1} \begin{pmatrix} \mathbf{I}_i \\ I_g \end{pmatrix} \tag{2}$$

Furthermore,

$$\mathbf{V}_i = \boldsymbol{S}(\boldsymbol{B}\boldsymbol{Z}^{-1}\boldsymbol{B}^T)^{-1}\boldsymbol{S}^T\mathbf{I}_i \tag{3}$$

yielding the equivalent impedance matrix of the signal lines in the interaction region (as shown in Figure 1(c)):

$$\boldsymbol{Z}_{eq} = \boldsymbol{S}(\boldsymbol{B}\boldsymbol{Z}^{-1}\boldsymbol{B}^T)^{-1}\boldsymbol{S}^T \tag{4}$$

$\boldsymbol{S}$ is an incidence matrix. Each column of $\boldsymbol{S}$ corresponds to a signal line or aggregate of power-ground lines; each row of $\boldsymbol{S}$ corresponds to a signal line. The element of the ith column and jth row of $\boldsymbol{S}$ is 1 if the column and row correspond to the same signal line; it is -1 if the column corresponds to the power-ground aggregate and the row corresponds to the associated signal line of the same cluster. In section 4, we show how this (frequency-dependent) impedance is represented in the SPICE extracted netlist.

3 Magnetostatic substrate loss modelling

There are two basic approaches one could take to modelling the substrate. One could mesh the substrate based on a volume filament approach[22], modelling the substrate as (in general) a coupled RLCK mesh (i. e., a full PEEC model, tantamount to a full-wave solution withing the quasi-static approximation[11]) The advantage of this technique is that it is very accurate since all 3D effects can be handled (e. g., differences in substrate effects due to well diffusions and the influence of well or substrate plugs). Substrate losses can be accurately modelled in both the electrostatic and magnetostatic problems, and their interactions are also modelled. The main disadvantage to this approach, despite its accuracy, is that extractions will be "clogged" with complex substrate networks. As in the case of explicit treatment of power-ground, it will quickly result in a computational intractable problem for all but the most trivial problem sizes. An alternative is to treat the substrate *implicitly* by means of a Green's function treatment and combine this with the implicit power-ground treatment of return-limited inductance extraction.

To consider substrate effects, we return to Maxwell's equations. Ignoring the displacement term (quasi-static approximation), the magnetic field is determined by:

$$\nabla \times \boldsymbol{B} = \mu\boldsymbol{J} \tag{5}$$

where the current density $\boldsymbol{J} = \sigma\boldsymbol{E} + \boldsymbol{J}_{src}$, where $\boldsymbol{J}_{src}$ is the applied current density. The (time-harmonic) fields are related to the scalar and vector potentials by:

$$\boldsymbol{E} = -j\omega\boldsymbol{A} - \nabla\phi \tag{6}$$

$$\boldsymbol{B} = \nabla \times \boldsymbol{A} \tag{7}$$

Using equations 6 and 7 (and Coulomb gauge) in equation 5 yields the following relation for the magnetic vector potential:

$$\nabla^2\boldsymbol{A} = j\mu\omega\sigma\boldsymbol{A} - \mu\boldsymbol{J}_{src} - \mu\sigma\nabla\phi \tag{8}$$

If we can assume the substrate is well plugged to a low-impedance power-ground distribution, it can be regarded as an equipotential and the last term on the right-hand-side of equation 8 can be ignored. All of the voltage induced (magnetically) in the substrate is dropped across the resistance of the substrate (or equivalently, the eddy currents of the substrate are sourced losslessly). With this assumption, capacitances to the substrate can be regarded as capacitances to the ideal ground reference, as is done for the case of capacitors coupled to the power-ground distribution. This leads to an implicit treatment of the substrate that is equivalent to that applied to the power-ground nets. This treatment ignores losses as displacement currents in the substrate are collected by plugs. The solution of equation 8 may then be written in integral form as:

$$\boldsymbol{A}(\boldsymbol{r}) = \mu\int_V \boldsymbol{J}_{src}(\boldsymbol{r}')G(\boldsymbol{r},\boldsymbol{r}')d^3\boldsymbol{r}' \tag{9}$$

where $G(\boldsymbol{r},\boldsymbol{r}')$ is the Green's function, found by solving the following equation:

$$\nabla^2 G(\boldsymbol{r},\boldsymbol{r}') = -\delta(\boldsymbol{r}-\boldsymbol{r}') + j\mu\omega\sigma G(\boldsymbol{r},\boldsymbol{r}') \tag{10}$$

From equation 9, the Green's function allows one to calculate the magnetic field at the field point $\boldsymbol{r}$ as a result of a current at the source point $\boldsymbol{r}'$.

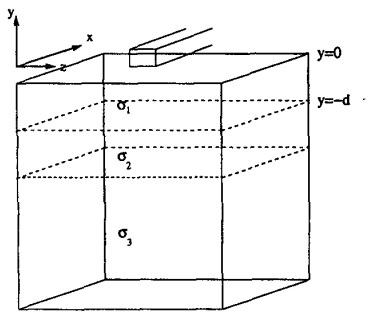

Figure 2: Multilayer substrate. Metal layers are routed in layer 0. $y = 0$ defines the substrate-oxide interface.

If one assumes a multilayer substrate stretching horizontally to infinity as shown in Figure 2, then axial symmetry applies and equation 10 can be reduced to a two-variable problem in cylindrical coordinates. Because this treatment assumes a uniform two-dimensional substrate profile, three-dimensional features such as substrate laminations sometimes used to reduce eddy current losses cannot be modelled. The spectral-domain transform can then be reduced to a one-dimensional Hankel transform[23]. We instead choose to keep the Green's function in Cartesian coordinates because we compute the filamentary inductance in the spectral domain, where axial symmetry no longer applies, before computing the transformation to spatial coordinates with a two-dimensional FFT. This provides us with a mechanism for a quick precharacterized look-up table for determining inductances directly in the presence of a uniform multilayer substrate.

If the source point (x', y', z') and field point (x, y, z) are in the top oxide layer, denoted as $k = 0$, it is straightforward to show that the Green's function between points in layer 0 can be expressed as the double integral,

$$G(r,r') = \int_0^\infty dm \int_0^\infty dn cos(mx)cos(mx')cos(nz)cos(nz') \times \frac{\left(\beta_0^u e^{\gamma_{mn}^0 max(y,y')} + \Gamma_0^u e^{-\gamma_{mn}^0 max(y,y')}\right)}{2\pi^2 \gamma_{mn}^0 (\beta_0^l \Gamma_0^u - \beta_0^u \Gamma_0^l)} \times \left(\beta_0^l e^{\gamma_{mn}^0 min(y,y')} + \Gamma_0^l e^{-\gamma_{mn}^0 min(y,y')}\right) \tag{11}$$

where ${\gamma_{mn}^k}^2 = m^2 + n^2 + j\omega\sigma_k\mu$. σ_k is the conductivity of layer k and μ is the permeability of free-space (all the materials are assumed to be non-magnetic). $\beta_0^{u,l}$ and $\Gamma_0^{u,l}$ are coefficients determined by satisfying the appropriate boundary conditions at each material interface. This follows from similar derivations for the electrostatic problem[24, 25].

As shown in Figure 2, $y = 0$ defines the oxide-silicon interface. To satisfy the requirement that the Green's function remain bounded as $y \to \infty$, $\beta_0^u = 0, \Gamma_0^u = 1$. Furthermore, if the bottom layer of the substrate (layer M) extends to $y \to -\infty$, $\beta_M^l = 1$ and $\Gamma_M^l = 0$.[2] With d_k being the y-distance to the interface between substrate layers k and $k+1$, the values of β_0^l and Γ_0^l can be found from the recursive formula

$$\begin{pmatrix} \beta_k^l \\ \Gamma_k^l e^{-2\gamma_{mn}^k d_k} \end{pmatrix} = \boldsymbol{A} \begin{pmatrix} \beta_{k+1}^l \\ \Gamma_{k+1}^l e^{-2\gamma_{mn}^k d_{k+1}} \end{pmatrix} \tag{12}$$

where the elements of $\boldsymbol{A}$ are given by:

$$\boldsymbol{A} = \begin{pmatrix} a & b \\ b & a \end{pmatrix}$$

and a, b are expressed as

$$a = \frac{1}{2}\left(1 + \frac{\gamma_{mn}^{k+1}}{\gamma_{mn}^k}\right) e^{(\gamma_{mn}^{k+1} - \gamma_{mn}^k)d_k}$$

$$b = \frac{1}{2}\left(1 - \frac{\gamma_{mn}^{k+1}}{\gamma_{mn}^k}\right) e^{(\gamma_{mn}^{k+1} - \gamma_{mn}^k)d_k}$$

We have found this formulation to be numerically robust.

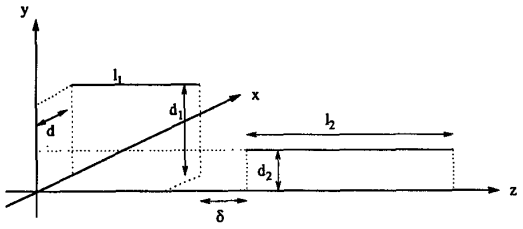

Figure 3: Geometry and spacings of the coupled filaments.

We now use this multilayer Green's function to derive the partial inductance for filamentary segments ("dressed" by the presence of the substrate). The current density of a filamentary current I at $y = d_1, x = 0, -l_1/2 \le z \le l_1/2$ in the z direction is given by:

$$\boldsymbol{J}(x',y',z') = I\delta(x')\delta(y'-d_1)\left[u(z'+l_1/2) - u(z'-l_1/2)\right]\hat{\boldsymbol{z}} \tag{13}$$

Figure 3 shows the geometry of the source filament and coupled filament for this calculation. Combining equations 9, 11, and 13 yields the following expression for the magnetic vector potential,

$$\boldsymbol{A}(x,y,z) = \hat{\boldsymbol{z}}\left(\frac{2\mu}{\pi^2}\right) \int_0^\infty dm \int_0^\infty dn cos(mx)cos(nz)\frac{sin(nl_1/2)}{n} \times \frac{\left(\beta_0^u e^{\gamma_{mn}^0 max(y,d_1)} + \Gamma_0^u e^{-\gamma_{mn}^0 max(y,d_1)}\right)}{\gamma_{mn}^0(\beta_0^l \Gamma_0^u - \beta_0^u \Gamma_0^l)} \times \left(\beta_0^l e^{\gamma_{mn}^0 min(y,d_1)} + \Gamma_0^l e^{-\gamma_{mn}^0 min(y,d_1)}\right) \tag{14}$$

Computing the mutual inductance to another filament at $y = d_2, x = d, l_1/2 + \delta \le z \le l_1/2 + \delta + l_2$ (see Figure 3)

$$M = \int_{l_1/2+\delta}^{l_1/2+\delta+l_2} A(d, d_2, z')dz' \tag{15}$$

yields,

$$M = \left(\frac{2\mu}{\pi^2}\right) \int_0^\infty dm \int_0^\infty dn cos(md)\frac{sin(nl_1/2)}{\gamma_{mn}^0 n} \times \frac{sin[n(l_1/2+\delta+l_2)] - sin[n(l_1/2+\delta)]}{n} \times \frac{\left(\beta_0^u e^{\gamma_{mn}^0 max(d_1,d_2)} + \Gamma_0^u e^{-\gamma_{mn}^0 max(d_1,d_2)}\right)}{(\beta_0^l \Gamma_0^u - \beta_0^u \Gamma_0^l)} \times \left(\beta_0^l e^{\gamma_{mn}^0 min(d_1,d_2)} + \Gamma_0^l e^{-\gamma_{mn}^0 min(d_1,d_2)}\right) \tag{16}$$

[2] For very high resistivity substrates, one could argue that the backside of the wafer must be modeled, for example, as an ideal ground place. If the backside were at $y = -D$, this would require that the Green's function (and the magnetic field) vanish for $y < -D$. We choose to model the substrate as infinitely thick in our context because of the presumption that other interconnect layers would always be present as a favored current return over a backside groundplane.

Equation 16 explicitly applies to filamentary currents. To extend this treatment to wires of finite cross section, we exploit the geometrical mean distance (GMD) approximation[26]. [3]. In the free-space case, $\beta_0^l = \Gamma_0^u = 1$ and $\beta_0^u = \Gamma_0^l = 0$ and this integral can be done exactly, to yield the well-known inductance formula of Grover[26].

We can approximate the integral of equation 16 by enclosing the x and z dimensions in a box of dimensions L_1 and L_2, respectively. Furthermore, we grid the substrate in x and z, so the L_1, L_2, d, l_1, l_2, and δ are integral multiplies of the grid spacing a. After some trigonometric manipulations, the summation becomes:

$$M = \frac{\mu}{2L_1L_2a^2}\sum_{m=1}^{L_1-1}\sum_{n=1}^{L_2-1} f_{mn} \times \left\{cos\left(\frac{m\pi d}{L_1}\right)cos\left(\frac{n\pi(l_1+\delta)}{L_2}\right) + cos\left(\frac{m\pi d}{L_1}\right)cos\left(\frac{n\pi(l_2+\delta)}{L_2}\right) - cos\left(\frac{m\pi d}{L_1}\right)cos\left(\frac{n\pi(l_1+l_2+\delta)}{L_2}\right) - cos\left(\frac{m\pi d}{L_1}\right)cos\left(\frac{n\pi\delta}{L_2}\right)\right\} \quad (17)$$

where f_{mn} is given by:

$$f_{mn} = \frac{\left(\beta_0^u e^{\gamma_{mn}^0 max(d_1,d_2)} + \Gamma_0^u e^{-\gamma_{mn}^0 max(d_1,d_2)}\right)}{(\beta_0^l\Gamma_0^u - \beta_0^u\Gamma_0^l)} \times \left(\beta_0^l e^{\gamma_{mn}^0 min(d_1,d_2)} + \Gamma_0^l e^{-\gamma_{mn}^0 min(d_1,d_2)}\right) \quad (18)$$

Defining $\tilde{M}_{uv}$ as:

$$\tilde{M}_{uv} = \frac{\mu}{2L_1L_2a^2}\sum_{m=1}^{L_1-1}\sum_{n=1}^{L_2-1} cos\left(\frac{m\pi u}{L_1}\right)cos\left(\frac{n\pi v}{L_2}\right) f_{mn} \quad (19)$$

equation 17 becomes:

$$M = \tilde{M}_{d,l_1+\delta} + \tilde{M}_{d,l_2+\delta} - \tilde{M}_{d,l_1+l_2+\delta} - \tilde{M}_{d,\delta} \quad (20)$$

$\tilde{M}_{uv}$ can be efficiently calculated by means of a fast Fourier transform (FFT) by creating an extended sequence y_{mn} from f_{mn} as follows:

$$y_{mn} = \begin{cases} f_{mn} & m = 0,\ldots L_1-1; n = 0,\ldots L_2-1 \\ f_{2M-m,n} & m = L_1,\ldots 2L_1-1; n = 0,\ldots L_2-1 \\ f_{m,2N-n} & m = 0,\ldots L_1-1; n = L_2,\ldots 2L_2-1 \\ f_{2M-m,2N-n} & m = L_1,\ldots 2L_1-1; n = L_2,\ldots 2L_2-1 \end{cases}$$

With this, $\tilde{M}_{uv}$ is given by:

$$\tilde{M}_{uv} = \frac{\mu}{8L_1L_2a^2}\sum_{m=1}^{2L_1-1}\sum_{n=1}^{2L_2-1} f_{mn} \times exp\left(\frac{im2\pi u}{2L_1}\right)exp\left(\frac{in2\pi v}{2L_2}\right) \quad (21)$$

For N metal layers, $N(N+1)/2$ FFTs are calculated as part of technology characterization (i. e., they only need to be calculated once and do not degrade the computational efficiency of the extraction engine) to provide look-up tables for $\tilde{M}_{uv}$ to allow calculation of M according to equation 20. It is well-known that a fine enough gridding must also be chosen (smaller a and more points in FFT) to cover adequate spectral content to achieve reasonable accuracy. This is particularly true for small values of d for which, M_{uv} has a (logarithmic) singularity. For the results presented here, we have chosen a as $0.25\mu m$ and a maximum interaction region size of $256\mu m \times 256\mu m$, requiring a 2048×2048 FFT. We post-process the FFT with a cubic-order interpolation formula[28], which allows us to achieve several percent accuracy down to the smallest filament spacing required for self-inductance calculation in the GMD approximation. This allows us to avoid the complexity of alternate solution techniques in the near field, the approach that is generally taken in more accurate field solvers[29].

[3] In Assura RCLX, we are still ignoring skin effect, assuming uniform current cross sections for wires. For frequencies beyond 10 GHz, it will certainly be necessary to modify this assumption through a volume filament decomposition or by means of an expansion to a more efficient basis[27]

4 Ladder network

To model the frequency dependence of equation 4 along with the frequency dependence of the substrate loss using frequency-independent elements (and, thereby, making the extracted netlist compatible with SPICE simulation), a ladder network as shown in Figure 4 is introduced for each signal line branch.

Representing all n signal branches within an interaction region, the current components become vectors, where each element of the vector corresponds to a different signal line. Consequently, $\boldsymbol{L_1}$, $\boldsymbol{L_2}$, $\boldsymbol{R_1}$, $\boldsymbol{R_2}$ are $n \times n$ matrices. $\boldsymbol{R_2}$ has off-diagonal elements, resulting in transresistances modelled in SPICE as current-dependent voltage sources.

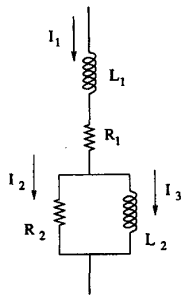

Figure 4: Ladder network for a signal segment.

The $n \times n$ impedance matrix of this reduced network is given by $\boldsymbol{Z}_{fit}$ where $\boldsymbol{V} = \boldsymbol{Z}_{fit}\boldsymbol{I}$ and $\boldsymbol{Z}_{fit} = \boldsymbol{R_1} + s\boldsymbol{L_1} + s\boldsymbol{L_2}(\boldsymbol{R_2} + s\boldsymbol{L_2})^{-1}\boldsymbol{R_2}$. We can now expand $\boldsymbol{Z}_{fit}$ in moments around $s = \infty$:

$$\boldsymbol{M_{-1}} = \boldsymbol{L_1}$$

$$\boldsymbol{M_0} = \boldsymbol{R_1} + \boldsymbol{R_2}$$

The moments of equation 4 can similarly be expanded around $s = \infty$ yielding:

$$\boldsymbol{M_{-1}} = \boldsymbol{SL'S^T}$$

$$\boldsymbol{M_0} = \boldsymbol{SL'BL^{-1}RL^{-1}B^TL'S^T}$$

where $\boldsymbol{L'} = (\boldsymbol{BL^{-1}B^T})^{-1}$. Note the $\boldsymbol{M_{-1}}$ and $\boldsymbol{M_0}$ correspond to the infinite-frequency inductance and resistance, respectively.

To incorporate the substrate correction and its associated frequency dependence, we recognize that in the presence of the substrate,

$$\boldsymbol{L} \rightarrow Re(\boldsymbol{L}_{substrate}(f_{max}))$$

and

$$\boldsymbol{R} \rightarrow R + Im(\boldsymbol{L}_{substrate}(f_{max}))2\pi f_{max}$$

where $\boldsymbol{L}_{substrate}$ is the complex dense complex partial inductance matrix constructed by FFT lookups from equation 20. We evaluate the correction at the user-specified frequency f_{max}.

Similarly, expanding the two lowest-order moments of $\boldsymbol{Z}_{fit}$ around $s = 0$ yields:

$$\boldsymbol{M}_0' = \boldsymbol{R}_1$$

$$\boldsymbol{M}_1' = \boldsymbol{L}_1 + \boldsymbol{L}_2$$

which correspond to the dc resistance and inductance, respectively. The moments of equation 4 can be similarly expanded around $s = 0$ yielding:

$$\boldsymbol{M}_0' = \boldsymbol{S}(\boldsymbol{B}\boldsymbol{R}^{-1}\boldsymbol{B}^T)^{-1}\boldsymbol{S}^T$$

$$\boldsymbol{M}_1' = \boldsymbol{S}(\boldsymbol{B}\boldsymbol{R}^{-1}\boldsymbol{B}^T)^{-1}\boldsymbol{B}\boldsymbol{R}^{-1}\boldsymbol{L}\boldsymbol{R}^{-1}\boldsymbol{B}^T(\boldsymbol{B}\boldsymbol{R}^{-1}\boldsymbol{B}^T)^{-1}\boldsymbol{S}^T$$

With the pseudoreturn, $\boldsymbol{M}_0'$ is simply the diagonal matrix of signal line resistances.

The fitting here is trivial. $\boldsymbol{M}_{-1}$ determines $\boldsymbol{L}_1$, $\boldsymbol{M}_0'$ determines $\boldsymbol{R}_1$, $\boldsymbol{M}_1'$ determines $\boldsymbol{L}_2$, and $\boldsymbol{M}_0$ determines $\boldsymbol{R}_2$. Specifically, $\boldsymbol{R}_2 = \boldsymbol{M}_0 - \boldsymbol{R}_1$ and $\boldsymbol{L}_2 = \boldsymbol{M}_1' - \boldsymbol{L}_1$

5 Comparisons with full-wave analysis

In order to validate our extraction results, we have developed a set of two-port ground-signal-ground (GSG) coplanar waveguide structures of the form shown in Figure 5 running over different substrates. These structures are simple enough to enable full-wave solution with Ansoft's HFSS engine, a finite-element solver, yielding S parameters. Ports are defined at the near-end and far-end. Structures like this can be easily fabricated and measured with microwave probes and a network analyzer (with proper reference deembedding structures)[8]. We similarly calculate the S-parameters from Spectre simulation of the Assura RCX SPICE netlist. Frequency-domain analysis is a far more precise means of accessing accuracy than time-domain simulations, since we can examine the accuracy with which high-frequency components are propagated and reflected, components that could in general be attenuated and lost as part of the Fourier spectrum of a "digital" time-domain waveform. We present the results for for a representative testcase here, a testcase which also demonstrate remaining sources of inaccuracy in the extraction.

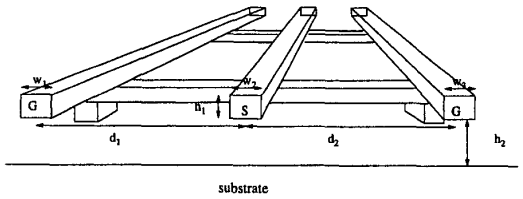

Figure 5: Simple GSG coplanar waveguide configurations for full-wave comparisons.

In this example, $h_1 = 0.5\mu m$, $h_2 = 2.715\mu m$, $w_1 = 2\mu m$, $w_2 = 4\mu m$, $w_3 = 10\mu m$, $d_1 = 30\mu m$, and $d_2 = 50\mu m$. The substrate is *very* heavily doped, $1m\Omega - cm$ (without even the lightly doped epitaxial layer which be required to construct devices), to accentuate the substrate effects. The ground lines are neither equal width nor equidistant from the signal lines, given an additional proximity-effect frequency dependence to the resistance and inductance. The ground lines are strapped every $500\mu m$ and the substrate is plugged from both ground lines every $500\mu m$. Figure 6 shows the S-parameter results from 50 MHz to 20 GHz in Smith chart form (although we have not sketched the contours of constant resistance and reactance that are commonly drawn on Smith charts). *HFSS* gives the HFSS result. *RL w/o ladder* gives the Assura RLCX result without any consideration of substrate or power-ground losses; this is the Assura RLCX result without the accuracy corrections described in this paper. *RL w/ ladder, no substrate* includes the power-ground losses but no effects from the substrate. *RL w/ ladder, substrate* includes substrate loss as well as power-ground loss. We comment that the HFSS results require in excess of 18 hours of compute time. The extraction in Assura and simulation in Spectre requires a couple of minutes.

S_{12} shows steadily better agreement with HFSS as loss mechanisms are added into the Assura extraction. Even with both substrate and power-ground losses considered, we are still underrepresenting the loss. We attribute this to the failure to consider the current-crowding skin and proximity effects in Assura. At 20 GHz, the skin depth is approximately $0.7\mu m$. Skin effects issues are actually mitigated in this testcase because of the comparatively large amount of current returning through the substrate, making the wire thickness rather than the width the more critical dimension for the skin effect. The S_{11} results also show similarly improving agreement as the accuracy features are added into the Assura extraction. High-frequency discrepancies in the real part of S_{11} are once again attributed to current-crowding effects.

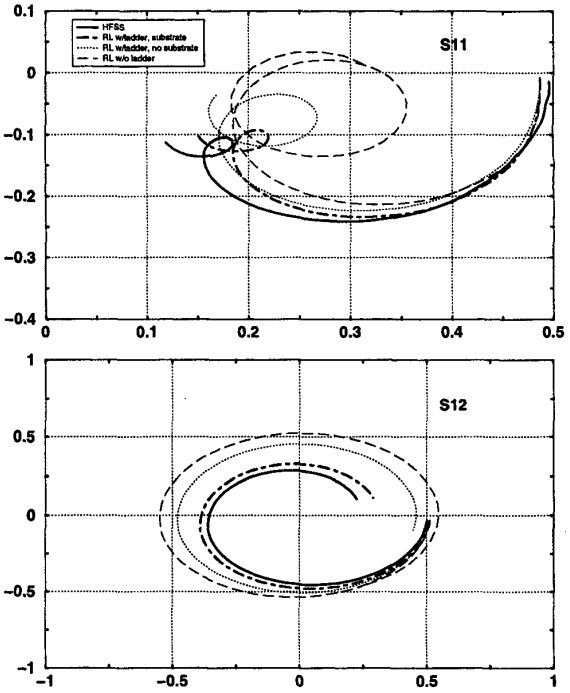

Figure 6: S parameters from 50 MHz to 20GHz for the coplanar ground-signal-ground testcase.

6 Conclusions

In this paper, we have described enhancements to the return-limited inductance extraction approach as implemented in Assura RCLX which handle losses in the power-ground and substrate. The approach is based on the design-driven assumption that the signal lines are routed within a low-impedance power-ground network and that the substrate is well plugged (or tapped) into this network. This allow *implicit* treatment of the effects of the substrate and power-ground distribution on signal line response, which can make signal-line extraction practical on a full-chip basis. Comparison with finite-element full-wave analysis shows the efficacy of these accuracy enhancements. To accurately model beyond 10 GHz, non-uniform current distributions across wire cross-sections will have to be supported in the extraction engine in a future enhancement.

References

[1] K. L. Shepard, D. Sitaram, and Y. Zheng. Full-chip, three-dimensional, shapes-based RLC extraction. In *Proceedings of the International Conference on Computer-Aided Design*, pages 142 – 149, 2000.

[2] P. J. Restle and et al. A clock distribution network for microprocessors. *IEEE Journal Solid-State Circuits*, 36:792 – 799, May 2001.

[3] S. Voinigescu and et al. Circuits and technologies for highly integrated optical networking IC's at 10 Gb/s to 40 Gb/s. In *International Custom Integrated Circuits Conference*, pages 331 – 338, 2001.

[4] K. W. J. Chew, S-F S. Chu, and C. C. C. Leung. Driving CMOS into the wireless communications arena with technology scaling. In *International Custom Integrated Circuits Conference*, pages 571 – 574, 2001.

[5] J. N. Burghartz, M. Soyuer, and K. A. Jenkins. Integrated RF and micrwave components in BiCMOS technology. *IEEE Transactions on Electron Devices*, 43:1559 – 1570, 1996.

[6] C. Patrick Yue and S. Simon Wong. On-chip spiral inductors with patterned ground shields for Si-based RF IC's. *IEEE Journal Solid-State Circuits*, 33:743 – 752, 1998.

[7] Ali M. Niknejad and R. G. Meyer. Analysis, design, and optimization of spiral inductors and transformers for Si RF IC's. *IEEE Journal Solid-State Circuits*, 33:1470 – 1481, 1998.

[8] B. Kleveland, C. H. Diaz, D. Vook, L. Madden, T. H. Lee, and S. S. Wong. Exploiting CMOS reverse interconnect scaling in multigigahertz amplifier and oscillator design. *IEEE Journal Solid-State Circuits*, 36:1480 – 1488, October 2001.

[9] Hui Wu and Ali Hajimiri. Silicon-based distributed voltage-controlled oscillators. *IEEE Journal Solid-State Circuits*, 36:493 – 502, March 2001.

[10] R. F. Harrington. *Field Computation by Moment Methods*. MacMillan, New York, 1968.

[11] A. E. Ruehli. Equivalent circuit models for three-dimensional multiconductor systems. *IEEE Transactions on Microwave Theory and Techniques*, MTT-22:216 – 221, March 1974.

[12] P. J. Restle, A. E. Ruehli, S. G. Walker, and G. Papadopoulos. Full-wave PEEC time-domain methods for the modeling of on-chip interconnects. *IEEE Trans. CAD*, 20:877 – 887, 2001.

[13] Hansruedi Heeb and Albert Ruehli. Retarded models for PC board interconnects – or how the speed of light affects your SPICE simulation. In *Proceedings of the IEEE/ACM International Conference on Computer Aided-Design*, pages 70 – 73, 1991.

[14] Keith Nabors and Jacob White. Fastcap: A multipole accelerated 3-D capacitance extraction program. *IEEE Trans. CAD*, 10(11):1447 – 1459, 1991.

[15] Mattan Kamon, Michael J. Tsuk, and Jacob K. White. FASTHENRY: A Multipole-Accelerated 3-D Inductance Extraction Program. *IEEE Transactions on Microwave Theory and Techniques*, 42(9):1750–1758, September 1994.

[16] S. Kapur and D. Long. IES^3: A fast integral equation solver for efficient 3-dimensional extractions. In *Proceedings of the IEEE/ACM International Conference on Computer Aided-Design*, pages 448 – 455, 1997.

[17] B. Krauter and L. T. Pileggi. Generating sparse partial inductance matrices with guaranteed stability. In *Proceedings of the International Conference on Computer-Aided Design*, pages 45 – 52, 1995.

[18] Kaushik Gala, David Blaauw, Junfeng Wang, Vladimir Zolotov, and Min Zhao. Inductance 101: analysis and design issues. In *ACM/IEEE Design Automation Conference*, pages 329 – 334, 2001.

[19] A. Devgan and et al. How to efficiently capture on-chip inductance effects: introducing a new circuit element K. In *Proceedings of the IEEE/ACM International Conference on Computer Aided-Design*, pages 150 – 155, 2000.

[20] M. W. Beattie and L. T. Pileggi. Modeling magnetic coupling for on-chip interconnect. In *ACM/IEEE Design Automation Conference*, pages 335 – 340, 2001.

[21] K. L. Shepard and Zhong Tian. Return-limited inductances: a practical approach to on-chip inductance extraction. *IEEE Trans. CAD*, April 2000.

[22] Y. Massoud and J. White. Simulation and modeling of the effect of substrate conductivity on coupling inductance. In *Proceedings of the IEDM*, pages 491 – 494, 1995.

[23] J. Zhao, W. Dai, R. C. Frye, and K. L. Tai. Green function via moment matching for rapid and accurate substrate parasitics evaluation. In *Proceedings of the IEEE Custom Integrated Circuits Conference*, pages 371 – 374, 1997.

[24] Ranjit Gharpurey and Robert G. Meyer. Modeling and analysis of substrate coupling in integrated circuits. *IEEE Journal Solid-State Circuits*, 31:344 – 353, March 1996.

[25] Ali M. Niknejad, Ranjit Gharpurey, and Robert G. Meyer. Numerically stable Green function for modeling and analysis of substrate coupling in integrated circuits. *IEEE Trans. CAD*, 17:305 – 315, April 1998.

[26] F. Grover. *Inductance Calculations: Working Formulas and Tables*. Dover, New York, 1962.

[27] L. Daniel, A. Sangiovanni-Vincentelli, and J. White. Using conduction modes basis functions for efficient electromagnetic analysis of on-chip and off-chip interconnect. In *ACM/IEEE Design Automation Conference*, pages 563 – 566, 2001.

[28] J. N. Lyness. Some quadrature rules for finite trigonometric and related integrals. In Patrick Keast and Graeme Fairweather, editors, *Numerical integration*, pages 17 – 33. D. Reidel Publishing Company, Dordrecht, 1987.

[29] J. Zhao, W. Dai, S. Kapur, and D. E. Long. Efficient three-dimensional extraction based on static and full-wave layered Green's functions. In *ACM/IEEE Design Automation Conference*, pages 224 – 229, 1998.